IEEE Access
Multidisciplinary | Rapid Review | Open Access Journal

Received July 31, 2019, accepted August 16, 2019, date of publication August 26, 2019, date of current version September 23, 2019.

Digital Object Identifier 10.1109/ACCESS.2019.2937587

Study of an Electromagnetic Ocean Wave Energy Harvester Driven by an Efficient Swing Body Toward the Self-Powered Ocean Buoy Application

YUNFEI LI[1], QIYU GUO[1], MANJUAN HUANG[1], XIN MA[2], ZHAOHUI CHEN[2], HUICONG LIU[1], (Member, IEEE), AND LINING SUN[1], (Member, IEEE)

[1]Jiangsu Provincial Key Laboratory of Advanced Robotics, School of Mechanical and Electric Engineering, Soochow University, Suzhou 215123, China
[2]Physical Oceanography Laboratory, Ocean University of China, Shandong 266071, China

Corresponding author: Huicong Liu (hcliu078@suda.edu.cn)

This work was supported in part by the National Natural Science Foundation of China under Grant 41527901, and in part by the Qingdao National Laboratory for Marine Science and Technology under Grant 2017ASKJ01.

ABSTRACT Ocean wave is one of the promising renewable energy sources all around the world. In this paper, an electromagnetic ocean wave energy harvester (OWEH) based on efficient swing body mechanism is presented. A swing body senses the ultra-low frequency wave motion and drive the rotor of an electromagnetic power module (EPM) rotating at high speed through transmission gears. A series of electromagnetic and dynamic simulations were carried out to optimize the power generation capability of the OWEH. Additionally, the power management circuit is specially designed such that the generated power is able to charge a lithium battery and discharge an external load automatically. The OWEH is installed inside an ocean buoy and tested in the Yellow China Sea. When the peak wave height is greater than 0.6 m, the maximum peak-to-peak output voltage is 15.9 V. The corresponding output power is as high as 0.13 W and the maximum power density is 0.21 mW/cm^3, where the internal resistance of the OWEH is 122 Ω. Due to the high performance and adaptability, the OWEH can potentially power many low power components, which opens a promising way for improving the life of ocean buoys. Considering the small dimension of $10 \times 10 \times 6.3$ cm^3, this OWEH can be mounted inside most buoys easily and realize the self-powered ocean buoys in the near future.

INDEX TERMS Ocean wave energy harvester (OWEH), swing body, electromagnetic, power management circuit, self-powered ocean buoy.

I. INTRODUCTION

Due to the global energy crisis, increased research efforts have been contributed to seek and develop the alternative energy resources to oil, such as solar, wind, ocean, biofuel energies and so on [1], [2]. Among all of the renewable energies, ocean wave energy is a promising one that has a huge potential and high power density. The ocean covers 70% of the Earth's surface and the total amount of the wave energy in the world is estimated to be 2 TW. Although the wave motion has the characteristics of randomness and ultra-low frequency, the feasibility of the ocean wave energy harvester (OWEH) has been numerically proposed and validated over the past decades [3], [4].

In the mid 1970s, the original methods of energy extraction applied in heaving buoys were proposed [5]. Based on the energy conversion approaches, there are three main categories of the energy harvesters [6], such as piezoelectric [7]–[16], triboelectric [17]–[21] and electromagnetic [5], [22]–[24]. In order to harvest the ultra-low frequency ocean wave energy, it is not preferable to implement traditional spring-mass-based resonant mechanisms [25]–[27]. Instead, the OWEHs usually utilize specific non-resonant inertial mechanisms, such as inertial balls [28]–[30], inertial sliders [31], [32] or inertial pendulum structures [33]. Chen *et al.* [34] designed a triboelectric OWEH by using the

The associate editor coordinating the review of this manuscript and approving it for publication was Tao Wang.

sway movement of an inertial ball. By using the collision of a rolling ball caused contact and separation, the triboelectric nanogenerator (TENG) converts the slow, random and high-force all-directional oscillatory motions into electricity. At the low vibration frequency of 2 Hz, the maximum output voltage, power and power density are 180 V, 64.8 mW and 75 μW/cm^3, respectively. Zhang *et al.* [35] proposed a sea snake structure with the TENG inside. Due to the action of the waves, multiple segments swing at a large angle, thereby accelerating the speed of the inertial ball in the device and improving the output. One segment of the TENG has the output voltage of 55 V and the power density of 3 W/m^2. Na *et al.* [36] designed a sliding rod type piezoelectric OWEH. The vibrating rod makes a reciprocating sliding, and repeatedly hits the piezoelectric benders on both sides, thereby converting the wave energy into electric energy. The average output voltage and power of the device are 2.42 V and 0.173 mW, respectively. Shao *et al.* [37] proposed a hybridized triboelectric-electromagnetic OWEH. The energy capturing mechanism is realized by moving the magnets through the relative sliding between the light bar and the bearing, thereby driving the electromagnetic and triboelectric parts for hybrid generation. At the frequency of 2 Hz, the output voltage and current generated by the triboelectric power generation module are 142 V and 23.3 μA, respectively. Yerrapragada *et al.* [38] designed an electromagnetic OWEH based on the inertial pendulum structure. The device uses a horizontal pendulum to capture the low frequency wave energy. When the operating frequency is 1 Hz and the external resistance is 110 Ω, the maximum output power is 4.79 mW. Ding *et al.* [39] also proposed an electromagnetic OWEH based on the inertial pendulum structure. In order to improve the energy conversion efficiency, the device additionally adds a gear acceleration mechanism. At the low vibration frequency of 0.3 Hz, the maximum output power and power density are 0.3 W and 0.2 mW/cm^3, respectively.

In view of the reported OWEHs with different energy capturing mechanisms, the inertial ball can capture multi-directional wave energy. However, it is mostly applicable to piezoelectric and triboelectric energy harvesters and the output power is generally low. The inertial slider can only capture the wave energy parallel to its sliding track, and hence the device has relatively poor energy efficiency. The inertial pendulum is able to capture complex and irregular wave energy. and convert the ultra-low frequency vibration ($<$1Hz) into continuous oscillation or rotation, where the energy conversion efficiency is relatively high. Therefore, this paper adopts an efficient swing body by using the inertial pendulum for the ultra-low frequency wave energy capturing. Thereafter, an electromagnetic power module (EPM) is utilized to rotating at high speed driven by the swing body through the transmission gears. Due to the high output performance and adaptability, the OWEH can charge the lithium battery and low power components for the potential ocean buoy applications.

II. DESIGN AND WORKING PRINCIPLE

This work aims to develop a high performance electromagnetic OWEH as an alternative power supply for the ocean buoy applications. The general architecture of the energy harvesting system is shown in Fig. 1. The device mainly consists of a swing body, an EPM, transmission gears and the outer frame. During operation, the OWEH is assembled inside the buoy platform. The irregular and ultra-low frequency ocean wave drives the buoy to sway, which can be regarded as the input energy source. Because of the inertia of the swing body, the relative rotation takes place between the swing body and the output frame of the OWEH. This rotation is strong in moment but small in amplitude, thus the transmission gears are used to accelerate the speed of the rotor. According to Faraday's law of electromagnetic induction, an induced electromotive force is generated in the coils of the EPM. Finally, the electricity can be stored in the lithium polymer battery through the charging circuit so as to power the warning lights, and sensors in the ocean buoys. Fig. 2 (a) shows the overall schematic view of the OWEH device with a dimension of 10 $\times$ 10 $\times$ 6.3 cm^3. The swing body made of two fan-shaped iron pendulum is assembled in a stepped shaft via two bearings and connected with the drive gear to transform the ultra-low frequency wave energy into the rotating mechanical energy. The moment of inertia mass of the swing body can be designed to adapt the wave spectrum. The radian, radius and thickness of the two fan-shaped iron pendulum are 60°, 40 mm, 10 mm and 120°, 40 mm, 15 mm, respectively. The EPM of Φ24 mm $\times$ 19 mm is embedded in a cylindrical cabinet of the housing. The drive gear is linked with the EPM through a driven gear and the transmission ratio between the drive and driven gears is 13.3. The EPM is composed of coils, magnets, iron core and outer casing. Three sets of coils are wound around the iron core and the shaft of the iron core is connected with the driven gear, which can be considered as a rotor. The number of turns and resistance of each coil are about 950 and 60 Ω, respectively. A pair of curved magnets with the radian of 140° and the height of 1.8 mm are symmetrically attached to the inner wall of the outer casing, which forms the stator. The photograph of the fabricated OWEH is shown in Fig. 2 (b).

III. SIMULATION AND OPTIMIZATION

A. ELECTROMAGNETIC SIMULATION OF THE EPM

When the EPM is driven to rotate, the magnetic flux across the coil changes and the induction electromotive force can be generated. In practical use, the rotation speed changes randomly because of the complexities of ocean waves. In order to optimize the structural dimensions of the EPM, electromagnetic analysis is carried out. Fig. 2 (c) shows the electromagnetic simulation model of the EPM in the JMAG software. Based on the model, the main parameters of the stator and rotor of the EPM are defined as the magnet curvature δ, the magnet thickness h, the thickness of the top of core c and the width of the root of the core a. In the simulation,

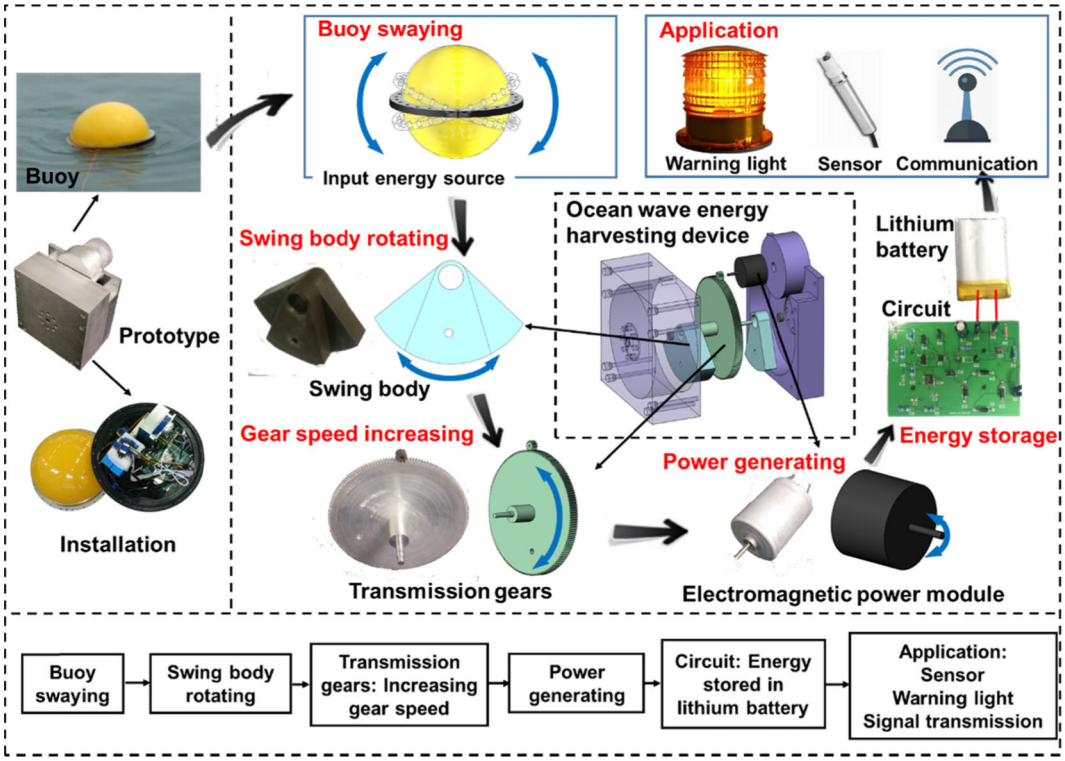

FIGURE 1. Architecture of the energy harvesting system.

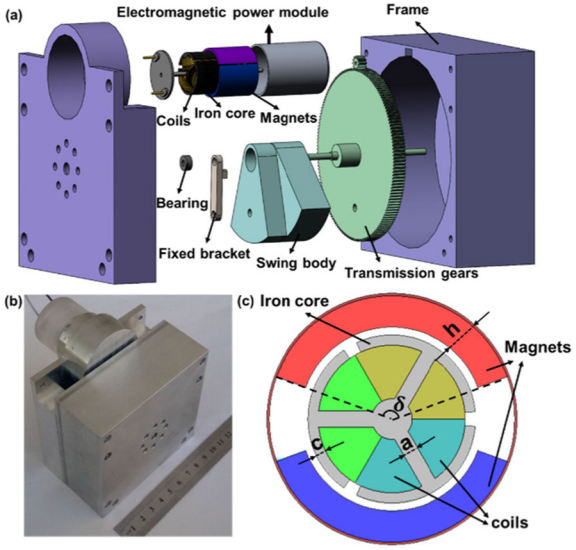

FIGURE 2. (a) Schematic diagram of the OWEH; (b) Photograph of the fabricated OWEH; (c) Electromagnetic simulation model of EPM.

the interval between the rotor and the stator is set as 0.5 mm, and the effective length of the model is 18 mm. The total volume of the winding coil is occupied about 70% of its accommodating space.

Fig. 3 (a) shows the voltage output diagram for different magnet curvature, at which the rotor speed is 800 r/min. The thickness of the magnet h is 1.8 mm, the width of the root of the core c is 1.5 mm and the thickness of the top of the core a is 1.5 mm. It can be seen that the highest voltage output can be achieved when the magnet has a curvature of 140°. Fig. 3 (b) shows the voltage output diagram for different magnet thicknesses. The magnet curvature is 140° and the other parameters are coincide with those in Fig. 3(a). The output voltage reaches the maximum value as the magnet thickness is 1.8 mm. The increase of the curvature and thickness of the magnet will increase the maximum value of the magnetic flux in the coil and thus increase the voltage output. However, when the curvature or thickness increases to a certain value, the distribution of the magnetic line will change. The maximum value of the magnetic flux in the coil will decrease and thus the voltage will be reduced. Therefore, the magnet of the stator can be determined with the curvature of 140° and thickness of 1.8 mm. By adjusting the thickness of the core top and the root width of the core, the rate of change of the magnetic flux in the coil is changed, so that the voltage changes accordingly. Fig. 3 (c) shows the voltage output for different core top thickness, where the other parameters are constant. It can be seen from the figure, the larger the value of core top thickness, the smaller the output voltage. Similarly, Fig. 3 (d) shows the voltage output for different core root width. As the root width of the core increases, the output voltage rises first and then decreases. The maximum output is obtained at 1.5 mm. Considering the iron core processing and the overall installation of the EPM, core top thickness and core root width in this design are both chosen to be 1.5 mm.

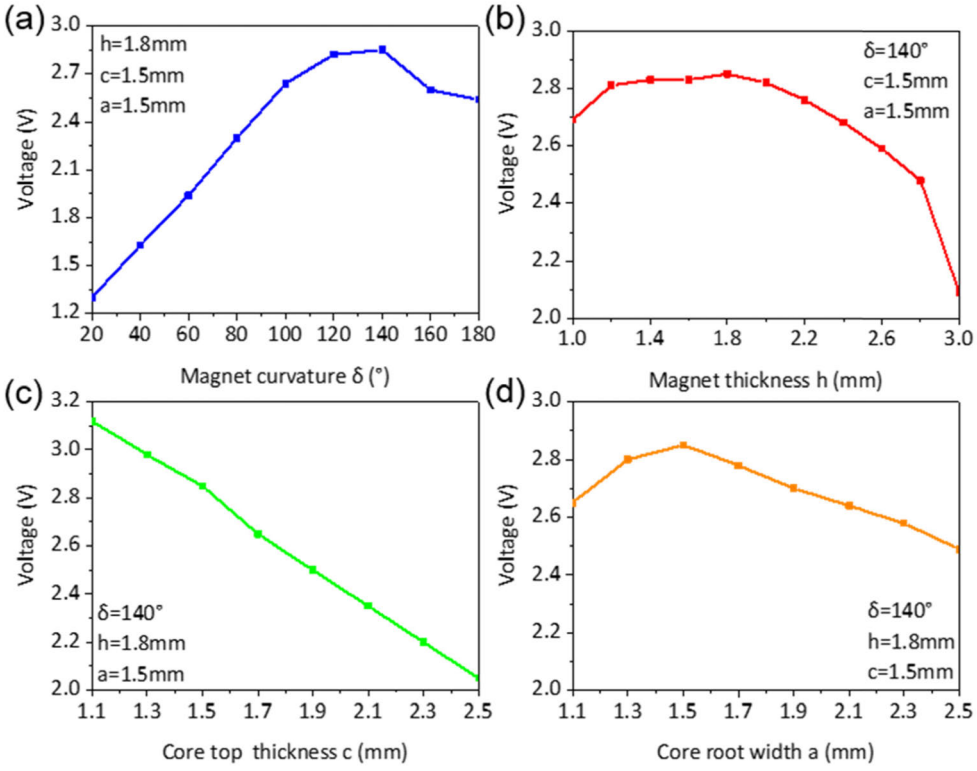

FIGURE 3. Simulated waveforms of the output voltage at different magnet curvature (a), magnet thickness (b), core top thickness (c) and core root width (d).

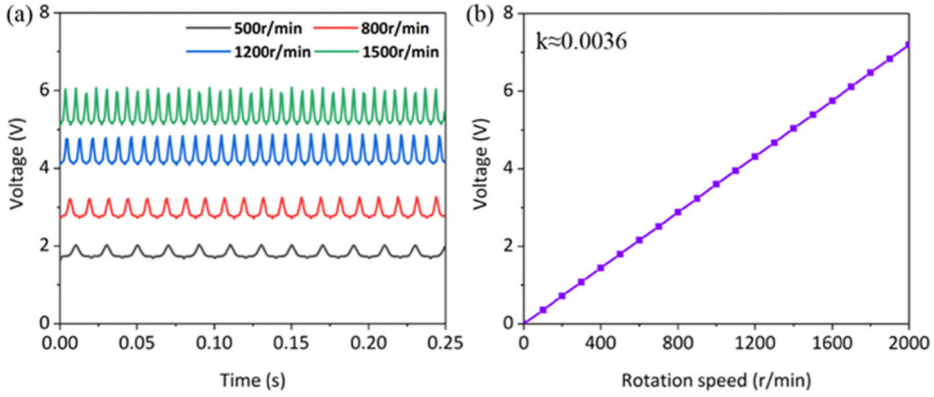

FIGURE 4. (a) Simulated waveforms of the output voltage at different rotation speeds; (b) Average output voltage at different rotation speeds.

To investigate the output performance of the EPM under various rotating speed, the dynamic simulation is carried out. Fig. 4 (a) shows the simulated waveforms of the open circuit voltage at rotation speeds of 500, 800, 1200 and 1500 r/min. The averaged output voltages from 0 r/min to 2000 r/min are calculated and plotted in Fig. 4 (b). It can be concluded that the output voltage and rotating speed can be approximated as a proportional function with a scale factor k of 0.0036.

B. DYNAMIC ANALYSIS OF THE OWEH

The dynamic model of the OWEH is shown in Fig. 5. The output voltage of the OWEH is largely determined by the rotating speed of the swing body. When the device is in regular or irregular movement of the wave (in Fig. 5 (b)), the swing body performs variable-speed sway. The Lagrangian method [40], [41] was used to derive the equation of the swing body movement. Fig. 5 (a) shows the initial state of the device. Under the action of the wave force, the position of the device changes accordingly, as shown in Fig. 5 (d). The pose transformation of the device from (a) to (d) can be regarded as a superposition of the movement transformation from the coordinate system XYZ to the coordinate system $X'Y'Z'$ and the rotation transformation from the coordinate system $X'Y'Z'$ to the coordinate system

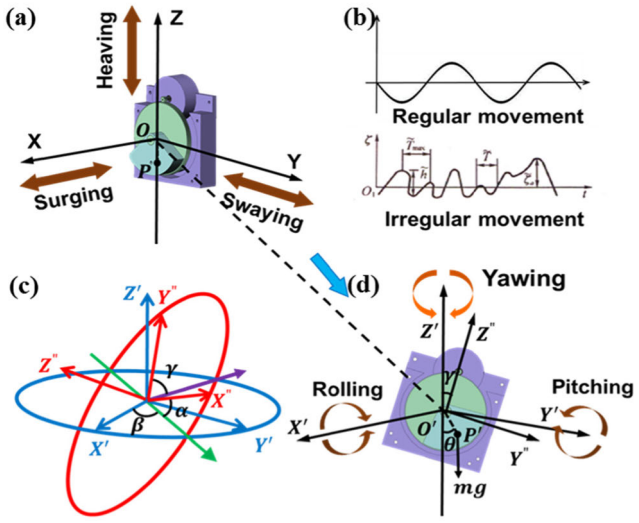

FIGURE 5. Schematic diagram of the OWEH: (a) initial position of the OWEH, (b) regular and irregular wave movement, (c) the sequence of the Euler angle and (d) position of the OWEH at a certain time.

$X''Y''Z''$ as shown in Fig. 5(c). Therefore, kinetic energy consists of translational and rotational components and is considered at the barycenter of the swing body:

$$\mathrm{T} = \frac{1}{2}m||v||^2 + \frac{1}{2}(I_{g-xy}\dot{\beta}^2 + I_{g-zy}\dot{\theta}^2 + I_{g-zx}\dot{\alpha}^2) \quad (1)$$

where m is the mass of the swing body and v is the speed vector of the barycenter of the swing body. I_{g-xy}, I_{g-zy} and I_{g-zx} are the moment of inertia of rotor about center of gravity on the Z', X' and Y' axis, respectively. $\dot{\beta}$, $\dot{\theta}$ and $\dot{\alpha}$ are the angular velocities of the swing body in the Z', X' and Y' directions, which is shown in Fig. 5 (c). Potential energy is also considered at the barycenter of the swing body:

$$V = mg\,(t_z - l\cos\alpha\cos\theta) \quad (2)$$

where t_z is the position of the center of the OWEH in Z direction and l is the eccentricity of the swing body. Fig. 5 (c) shows the sequence of the Euler angle of $Z'-Y'-X'$. When locating initial position P (0, 0, -l), the displacement function of the barycenter of the swing body can be expressed as:

$$\begin{aligned} &P'\left(x', y', z'\right) \\ &= PR_zR_yR_x + O'O \\ &= (0,0,-l)\begin{bmatrix} \cos\beta & \sin\beta & 0 \\ -\sin\beta & \cos\beta & 0 \\ 0 & 0 & 1 \end{bmatrix}\begin{bmatrix} \cos\alpha & 0 & -\sin\alpha \\ 0 & 1 & 0 \\ \sin\alpha & 0 & \cos\alpha \end{bmatrix} \\ &\quad\times\begin{bmatrix} 1 & 0 & 0 \\ 0 & \cos\theta & \sin\theta \\ 0 & -\sin\theta & \cos\theta \end{bmatrix} + \left(t_x, t_y, t_z\right) \\ &= \left(t_x - l\cos\alpha, t_y + l\cos\alpha\sin\theta, t_z - l\cos\alpha\cos\theta\right) \end{aligned} \quad (3)$$

where $O'O$ is the displacement vector of the center of the OWEH. And the velocity vector v can be derived from this displacement function. The Lagrangian is formed by $L = T - V$. In order to evaluate the effect of damping, the Rayleigh dissipation function R is used and the Euler–Lagrange equation can be expressed as:

$$\mathrm{R} = \frac{b}{2}(\dot{\theta} - \dot{\gamma})^2 \quad (4)$$

$$\frac{d}{dt}\left(\frac{dL}{d\dot{\theta}}\right) - \frac{dL}{d\theta} + \frac{dR}{d\dot{\theta}} = 0 \quad (5)$$

Therefore, the equation of motion of the swing body is derived as:

$$\begin{aligned} \left[m\,(l\cos\alpha)^2 + I_{g-zy}\right]\ddot{\theta} = &-ml\cos\alpha\,(\ddot{z}\sin\theta + \ddot{y}\cos\theta) \\ &+ 2ml^2\dot{\alpha}\dot{\theta}\cos\alpha\sin\alpha \\ &- mgl\cos\alpha\sin\theta - b\left(\dot{\theta} - \dot{\gamma}\right) \end{aligned} \quad (6)$$

The output voltage can be expressed as:

$$\mathrm{V} = k\left(\dot{\theta} - \dot{\gamma}\right) \quad (7)$$

According to Eqs. (6) and (7), a MATLAB/Simulink model is built to investigate the waveform of the output voltage. In this simulation, k is the proportional coefficient of output voltage, $\dot{\gamma}$ is the angular velocity of the OWEH and b represents the mechanical damping coefficient and electrical damping coefficient.

C. OPTIMIZATION OF THE SWING BODY

The swing body in this designed is a fan-shaped iron pendulum with a thickness of 2 cm. Under the excitation of irregular waves, the swing body of the OWEH will rotate or oscillate due to the action of gravity and inertia force, thereby capturing the wave energy. The irregular ocean wave can be regarded as a superposition of numerous sine waves as shown in Fig. 5(b). To simplify the dynamic model, the random motion of the OWEH is transformed into a sinusoidal motion in a two-dimensional plane as shown in Fig. 6.

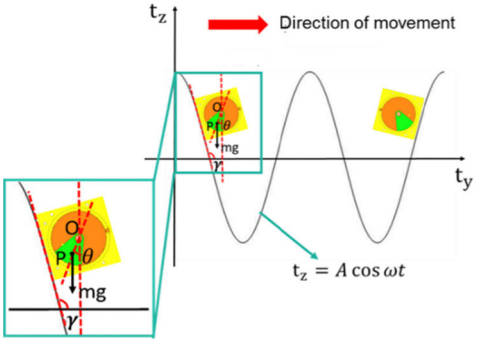

FIGURE 6. The OWEH motion model diagram in a two-dimensional plane.

The motion equations of the center of the swing body can be expressed as:

$$t_z = A\cos\omega t \quad (8)$$

$$\gamma = \arctan(\dot{t_z}) \quad (9)$$

$$t_y = t \quad (10)$$

$$\alpha = 0 \quad (11)$$

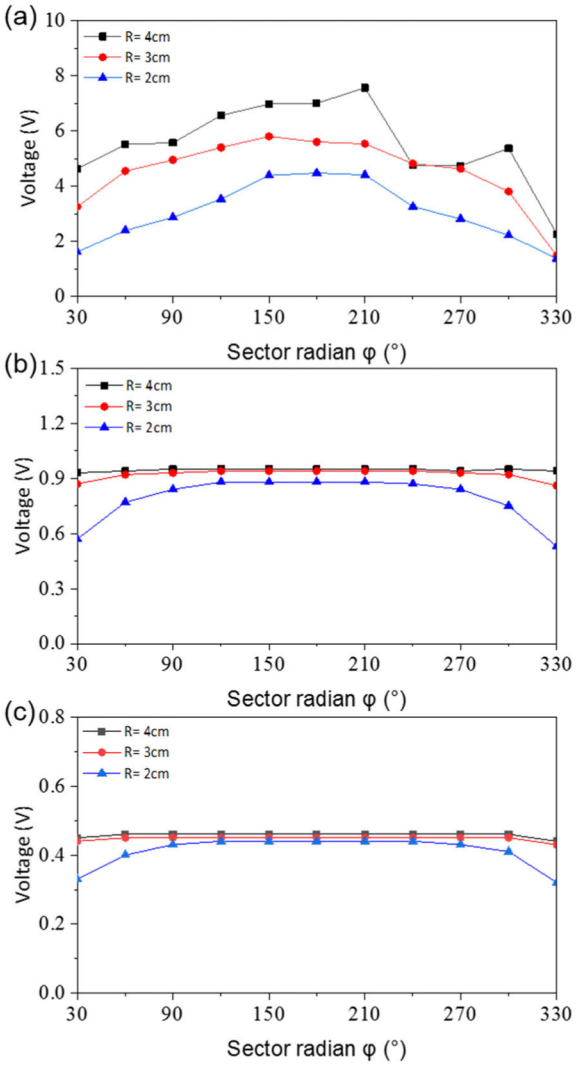

FIGURE 7. Simulated waveforms of the output voltage at the amplitude of 0.3 m and the period of 1 s (a), 2 s (b) and 3 s (c) with different sector radian and radius.

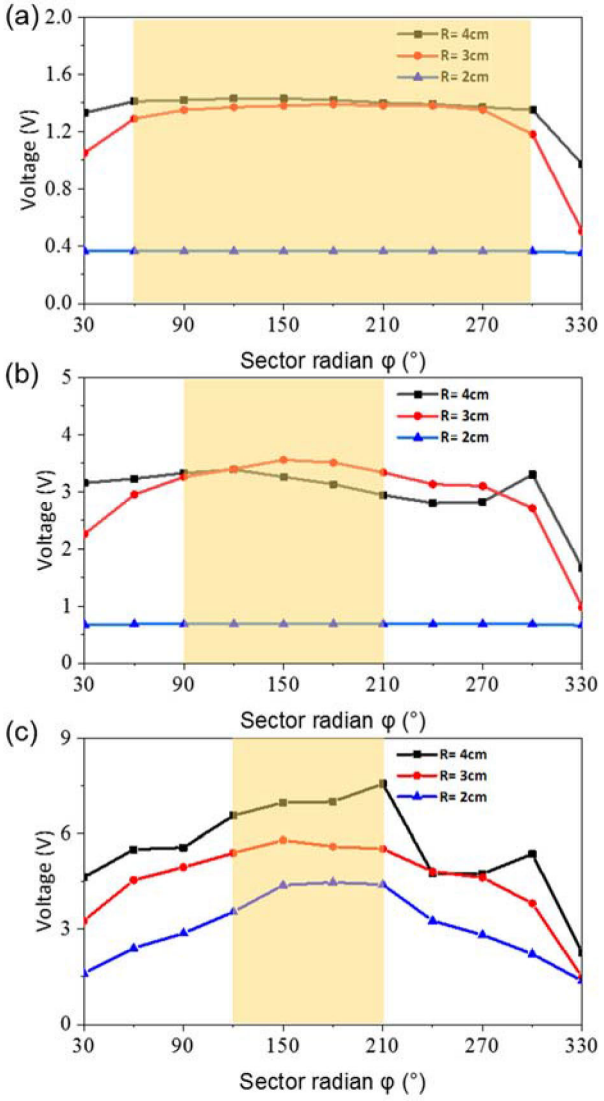

FIGURE 8. Simulated waveforms of the output voltage at the period of 1 s and the amplitude of 0.1 m (a), 0.2 m (b) and 0.3 m (c) with different sector radian and radius.

where A and ω is the amplitude and frequency of the sinusoidal motion, respectively. Therefore, the simplified dynamics equation is derived as:

$$\left(ml^2 + I_{g-zy}\right)\ddot{\theta} = -ml\ddot{i}_z \sin\theta - mgl\sin\theta - b\left(\dot{\theta} - \dot{\gamma}\right) \quad (12)$$

It can be seen that the speed of the swing body is related to the mass m, the moment of inertia I_{g-zy} and the eccentricity l of the swing body itself. The mass, the moment of inertia and the eccentricity of the swing body can be expressed by the following equations:

$$\mathrm{m} = \frac{1}{2}\rho\varphi R^2 d \quad (13)$$

$$l = \frac{4R\sin\frac{\varphi}{2}}{3\varphi} \quad (14)$$

$$I_{g-zy} = \frac{1}{2}mR^2 \quad (15)$$

where R, φ, d and ρ are the radius, radian, thickness and density of the swing body, respectively. Therefore, the optimal parameters of the device can be determined by varying the radius, radian, thickness and material density of the swing body.

Fig. 7 (a) (b) (c) show the relationship between the output voltage and the sector radian with different sector radius at wave amplitude of 0.3 m and wave periods of 1 s, 2 s, and 3 s, respectively. It can be seen from Fig. 7 (a) that when the period is 1 s, the output voltage of the device fluctuates greatly with the increasement of the sector radian. After the period exceeds 2 s, output voltage becomes stable and the voltage fluctuation range is within 0.3 V, as shown in Fig. 7 (b) and (c).

Fig. 8 (a) (b) (c) show the relationship between the output voltage and the sector radian with different sector radius at wave period of 1 s and wave amplitudes of 0.1 m, 0.2 m

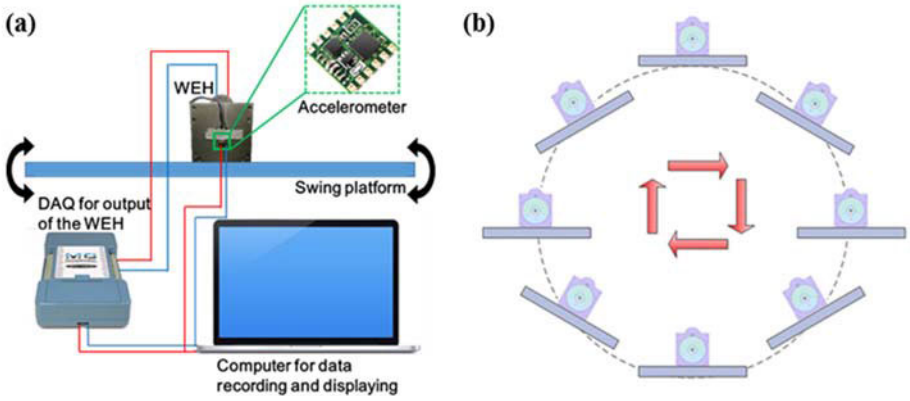

FIGURE 9. (a) Experimental setup of the OWEH; (b) Track diagram of the platform movement.

and 0.3 m, respectively. As can be seen, the output voltages at radius of 4 cm and 3 cm is significantly higher than that at a sector radius of 2 cm regardless of the sector curvature. When the amplitude is 0.1 m, 0.2 m and 0.3 m, the devices with radius of 3 cm and 4 cm can achieve higher output voltages between 120° and 210°. On the other hand, as the sector radian increases, the mass of the swing body will be increased accordingly, which affect the integration with the ocean buoy and increase the cost greatly. Taken into account of these factors, a fan-shaped swing body with radius of 4 cm and radian of 120° is designed, and a fan-shaped pendulum with a radius of 4 cm and a radian of 60° is added as a supplement. The final design of the compound swing body has a mass of 0.3 kg and an eccentricity of 2 cm. It can be obtained by simulation that when the period is 1 s, the output voltages at amplitudes of 0.1 m, 0.2 m, and 0.3 m are 1.43 V, 3.03 V and 7.38 V, respectively.

IV. EXPERIMENTAL CHARACTERIZATION

A. OPEN CIRCUIT VOLTAGE TEST

Fig. 9 (a) shows the experimental setup, consisting of a data acquisition card (DAQ), an accelerometer, a swing platform and a computer. The OWEH is placed on the swing platform to simulate the wave motion and the accelerometer is used to measure the rotation angles in X, Y and Z directions and the accelerations in X'', Y'' and Z'' directions. The output of the OWEH is connected to the DAQ. The computer is used to receive and store the data from the accelerometer and the DAQ. Fig. 9 (b) shows the track diagram of the platform movement.

Fig. 10 shows the output voltage of the OWEH under the rotation angle of about 30° in Y direction, vibration amplitude of 60 cm and periods of 1 s, 2 s and 3 s. Fig. 10 (a) (d) (g) show the waveforms of the rotation angle in X'' direction under the period of 1 s, 2 s and 3 s, respectively. Fig. 10 (b) (e) (h) show the waveforms of the accelerations in Z and Y directions under the periods of 1 s, 2 s and 3 s, respectively. And the acceleration on the Z axis does not contain gravitational acceleration. The simulation and experimental results of the output voltage under the period of 1 s, 2 s and 3 s are shown in Fig. 10 (c), (f) and (i), respectively. As can be seen that the experiment results of the output voltage are consistent with those simulated according to Eqs. (6) and (7). It can be seen that as the vibration period becomes shorter, the device output voltage becomes larger. When the vibration period is 1 s and the peak acceleration in the Z-axis direction is about 1 g, the maximum output voltage of the device is about 10.2 V. As the vibration period increases from 1 s to 2 s, the output voltage of the device drops significantly. When the period is changed from 2 s to 3 s, the output voltage of the device becomes even lower.

Fig. 11 (a) (b) (c) are the simulated and experimental voltage waveforms of the device at vibration amplitude of 0.2 m and periods of 1 s, 2 s and 3 s, respectively. Similarly, Fig. 11 (d) (e) (f) show the voltage waveforms of the device at vibration amplitude of 0.1 m and periods of 1 s, 2 s and 3 s, respectively. It can be seen that the dynamic simulation of the OWEH is consistent with the experimental results. When the vibration amplitude is 0.2 m and the periods are 1 s, 2 s and 3 s, the maximum output voltages of the device are 7.69 V, 2.02 V and 1.02 V, respectively. When the vibration amplitude is changed to 0.1 m, the maximum output voltages of the device become 5.59 V, 1.56 V and 0.79 V, respectively, at the vibration periods of 1 s, 2 s and 3 s. Comparing with the output voltages in Figs. 10 and 11, it can be concluded that when the period is constant, the larger the amplitude, the higher the output voltage of the device. And the maximum output voltage of the device is positively correlated with the amplitude, which is also consistent with the simulation results.

B. BATTERY CHARGING TEST

Since the current and voltage produced by the OWEH is unsteady, it is unsuitable for either charging a battery or supplying power directly. A power management circuit is designed so as to produce a stable power input to the battery. Fig. 12 (a) shows the circuit diagram of the power management system, consisting of the OWEH device, a rectifier circuit, a charging and discharging circuit, an external load and a lithium polymer battery of 50 mAh. The OWEH

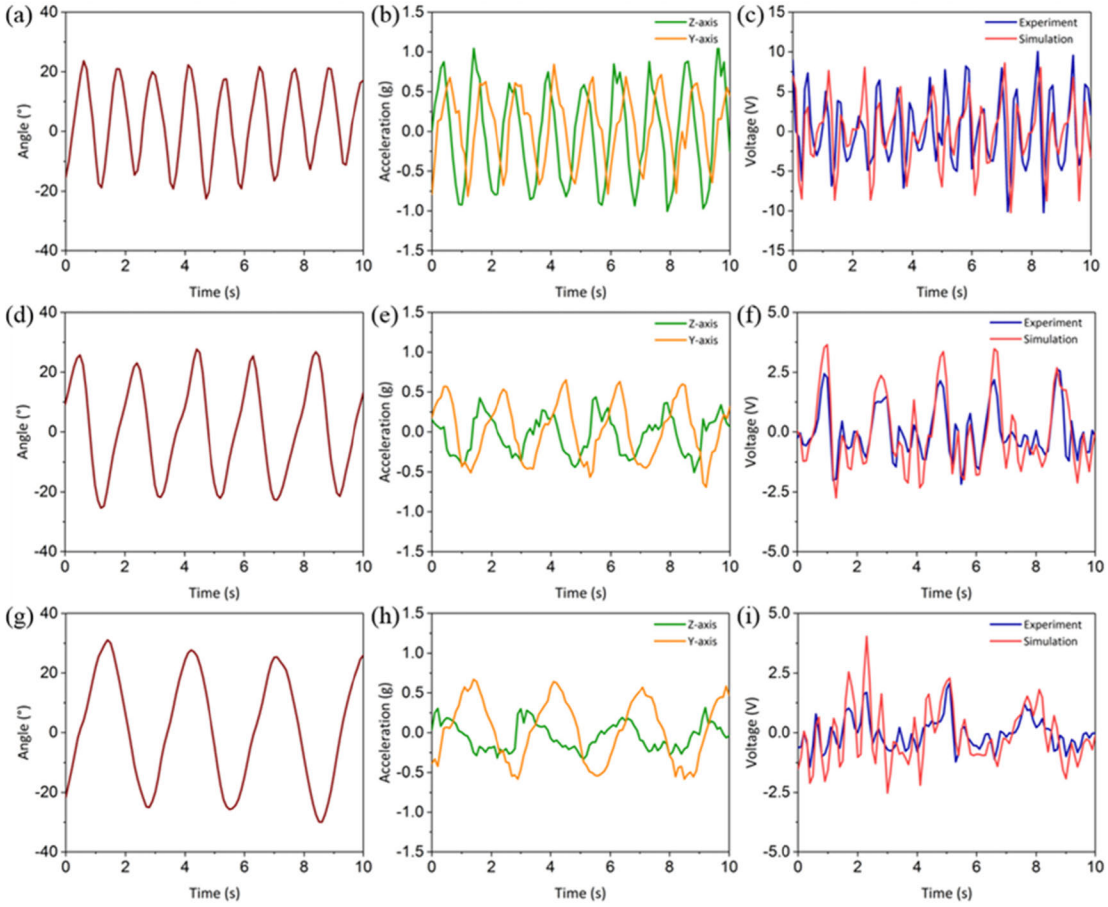

FIGURE 10. Angle of rotation in X" direction, accelerations in Z and Y directions and output voltage at the amplitude of 0.3 m and period of 1 s (a) (b) (c), the amplitude of 0.3 m and period of 2 s (d) (e) (f) and the amplitude of 0.3 m and period of 3 s (g) (h) (i).

working as an AC power supply harvests wave energy and generates alternating current. Then the input AC power is rectified by the rectifier circuit and flows to the lithium polymer battery through the charging circuit. The charging circuit is mainly based on the commercial integrated circuit, LTC4071, which can prevent excessive charging current and protect the lithium polymer battery from permanent damage due to deep discharge [42]–[44]. It can also offer float voltage of 4.1 V. In order to control the charging and discharging time of the lithium battery and meet the working voltage of the power supply components, the discharge circuit is designed based on the LTC1540 and MAX4685 chips [45], [46], which determines the voltage across the polymer lithium battery by adjusting the resistance values of R_H, R_L, R_Y, R_1 and R_2. When the voltage reaches a threshold of 4.1 V, the polymer lithium battery starts to discharge to the load.

Fig. 13 shows the voltage across the battery and the external load during the charging process. The upper voltage threshold of the polymer lithium battery is set as 4.1 V, and the lower voltage threshold is 2.8 V. The experiment contains 3 cycles of charging and discharging process. Each cycle can be divided into two parts. Stage 1 is the charging process, where the voltage across the lithium polymer battery gradually increases from 3.0 V to 4.1 V. The battery is in an open state, and the discharge circuit monitors the voltage across the battery. In stage 2, the lithium polymer battery is connected to the load of 100 Ω through the discharging circuit and the voltage across the battery drops to 3.6 V within 5 s. Then, the voltage across the battery drops from 3.6 V to 3 V and the voltage across the external load drops from 3.2 V to 2.8 V.

C. IN-OCEAN TEST

To validate the output performance of the proposed OWEH design under the real ocean wave condition, an in-ocean test was conducted on September 14th, 15th and 16th, 2018 in Qingdao. The research boat (shown in Fig. 14 (d)), DONG FANG HONG 2, was used to carry the prototype to the Yellow China Sea (120.303E, 36.043N). Fig. 14 (b) shows the installation of the OWEH inside a small wave buoy. The buoy is an elliptical sphere with two layers of internal space. Thus, the underlying space can hold the heavy block to adjust the center of gravity and the upper space is used to place an OWEH prototype, a battery source and a DAQ card. Since the

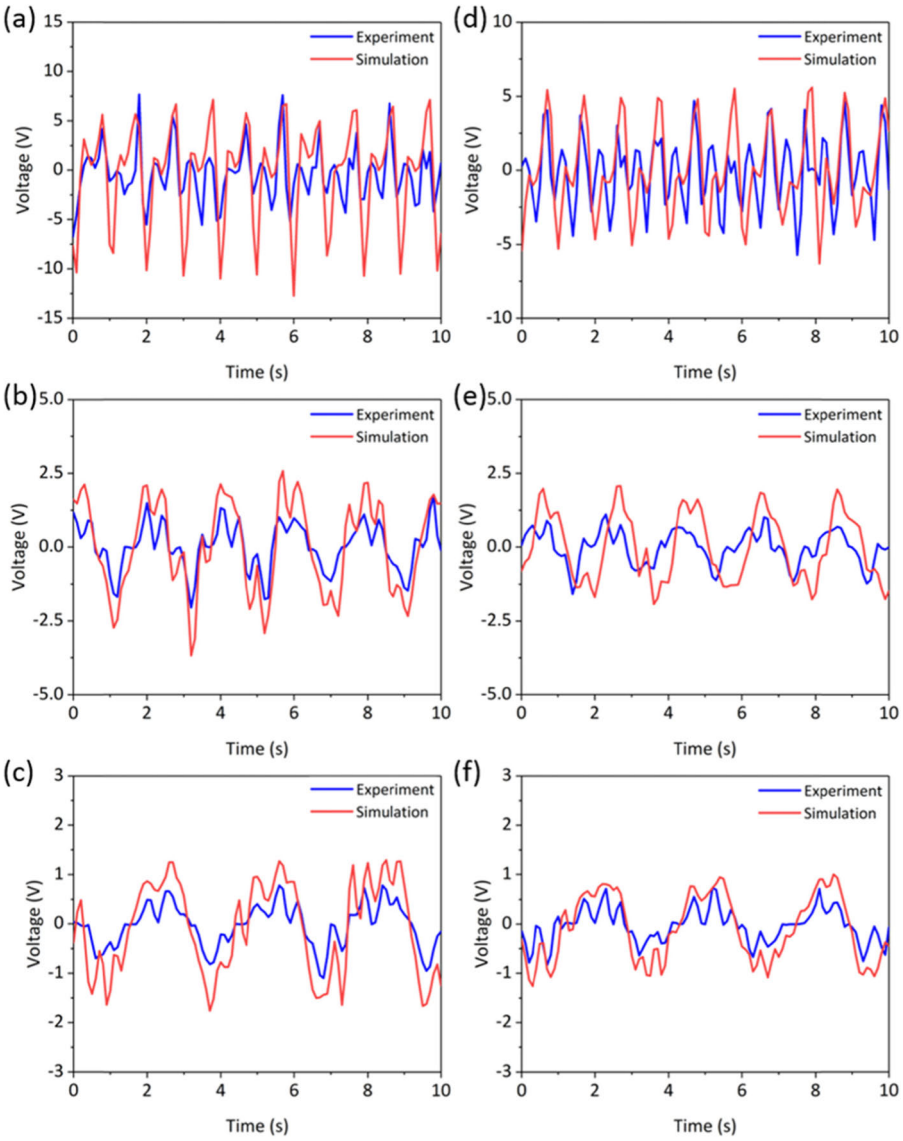

FIGURE 11. Experiment and simulation results at the amplitude of 0.2 m and period of 1 s (a), 2 s (b), 3 s (c) and the amplitude of 0.1 m and period of 1 s (d), 2 s (e), 3 s (f).

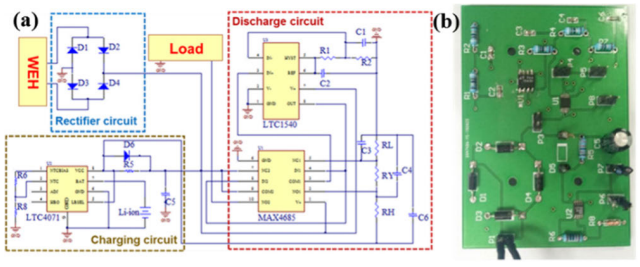

FIGURE 12. (a) Circuit diagram; (b) Photograph of the power management system.

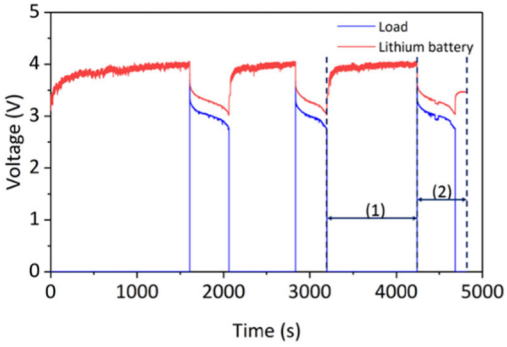

FIGURE 13. Voltage across the battery and load in the power management circuit during the charging and discharging process.

in-ocean test is conducted for about 72 hours continuously, the DAQ card is used to read and store the output voltage data of the OWEH and the battery is used to supply power to the DAQ card. The real scene of the in-ocean test is shown in Fig. 14 (c). During the experiment, two buoys are used, one for wave data collection and the other for voltage data acquisition of the OWEH.

TABLE 1. Output characteristics table of the published OWEHs in recent years.

Author	Captive energy mechanism	Energy conversion approach	Volume (cm*cm*cm)	Output power density	Working frequency
Hwang[30]	The inertial ball	Piezoelectric	3.8*1.9*0.2	47.85μW/cm^3	0.5Hz
Chen[34]	The inertial ball	Triboelectric	6*12*12	0.075mW/cm^3	2 Hz
Xu[31]	The inertial slider	Triboelectric	4.5*7.5*22.8	0.013mW/cm^3	2.9 Hz
Yerrapragada[38]	The inertial pendulum	Electromagnetic	76.1*12.7*20.3	0.24μW/cm^3	1 Hz
Ding[39]	The inertial pendulum	Electromagnetic	1508(cm^3)	0.2mW/cm^3	0.03 Hz
This paper	The inertial pendulum	Electromagnetic	10*10*6.3	0.21mW/cm^3	Random in-ocean

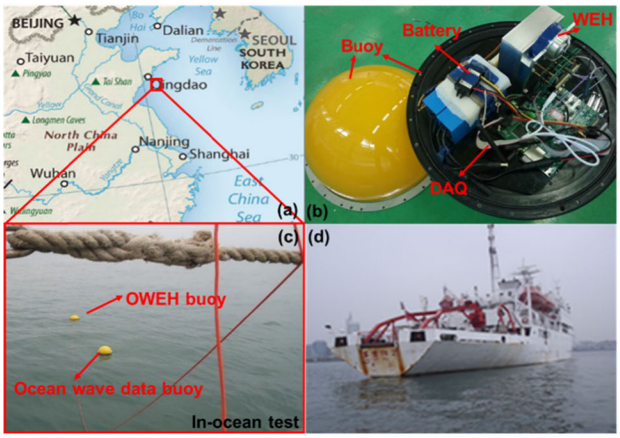

FIGURE 14. In-ocean test of the OWEH: (a) the location of experiment, (b) the installation, (c) the in-ocean test and (d) the research boat.

Analysis of the wave data within three days shows that the peak wave height is mainly concentrated in 0.2 m∼0.8 m. According to the wave height, it is roughly divided the ocean wave conditions into small, medium and large, which are a maximum peak wave height of less than 0.4 m, between 0.4 m and 0.6 m, and more than 0.6 m, respectively. Fig. 15 (a) shows the wave height curves for different ocean conditions taken from the wave buoy. The corresponding open circuit voltage output taken from the energy harvesting buoy is shown in Fig. 15 (b). According to Eqs. 6 and 7, the output performance of the device is mainly determined by the wave height in the ultra-low frequency ocean environment. Therefore, the larger the wave height, the higher the device output. At the larger wave condition, the angular velocity of the swing body is faster and the maximum peak-to-peak output voltage is 15.9 V. The corresponding output power is 0.13 W and the maximum power density is 0.21 mW/cm^3, where the internal resistance of the OWEH is 122 Ω. Comparing the wave energy harvesting devices reported in Table 1, the power density of the OWEH in this work is much better. Meanwhile, it shows high adaptability of irregular direction and ultra-low frequency vibration in real ocean wave environment.

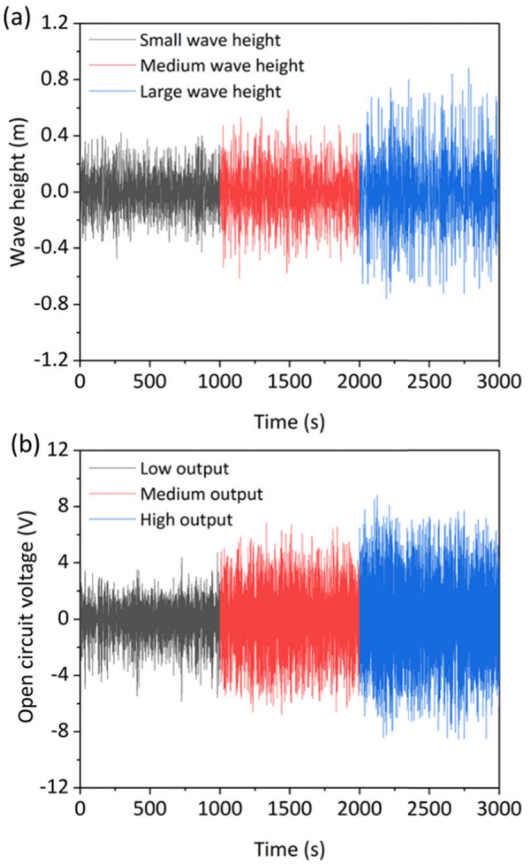

FIGURE 15. (a) Waveforms of the wave height under different ocean conditions; (b) Waveforms of the output voltage under different ocean conditions.

V. CONCLUSION

In summary, this paper presents the preliminary study of an electromagnetic OWEH based on the efficient swing body mechanism. A series of electromagnetic simulations are carried out to optimize the structure of the EPM and analysis the output performance with different rotating speed. Additionally, the dynamic model of the OWEH is created to optimize the structure size of the swing body and predict its power

generation capability. The correctness of the dynamic model is verified by designing a prototype and testing it in the swing platform. Experimental results show good agreement with simulation results. In the open circuit voltage test, it is found that the harvesting performance of the OWEH is positively correlated with the wave height and the square of the wave frequency. Additionally, the integration of ocean buoy and OWEH is realized. The in-ocean test proves that the OWEH can harvest ultra-low frequency and irregular wave energy, and has the high output performance of 0.13 W in power and 0.21 mW/cm^3 in power density. The ocean wave energy harvesting approach opens a promising way for extending the life of ocean buoys in the future.

ACKNOWLEDGMENT

(Yunfei Li and Qiyu Guo contributed equally to this work.)

REFERENCES

[1] M. A. Mustapa, O. B. Yaakob, Y. M. Ahmed, C.-Y. Rheem, K. K. Koh, and F. A. Adnan, "Wave energy device and breakwater integration: A review," *Renew. Sustain. Energy*, vol. 77, pp. 43–58, Sep. 2017.

[2] R. Alamian, R. Shafaghat, S. S. Hosseini, and A. Zainali, "Wave energy potential along the southern coast of the Caspian Sea," *Int. J. Mar. Energy*, vol. 19, pp. 221–234, Sep. 2017.

[3] L. Wang, J. Isberg, and E. Tedeschi, "Review of control strategies for wave energy conversion systems and their validation: The wave-to-wire approach," *Renew. Sustain. Energy Rev.*, vol. 81, pp. 366–379, Jan. 2018.

[4] Z. Wang, "New wave power," *Nature*, vol. 542, no. 7640, pp. 159–160, 2017.

[5] C. A. Diamond, C. Q. Judge, B. Orazov, Ö. Savaş, and O. M. O'Reilly, "Mass-modulation schemes for a class of wave energy converters: Experiments, models, and efficacy," *Ocean Eng.*, vol. 104, pp. 452–468, Aug. 2015.

[6] A. Tunde and H. Li, "Ocean wave energy converters: Status and challenges," *Energies*, vol. 11, no. 5, p. 1250, 2018.

[7] Z. Lin and Y. Zhang, "Dynamics of a mechanical frequency up-converted device for wave energy harvesting," *J. Sound Vib.*, vol. 367, pp. 170–184, Apr. 2016.

[8] Z. Yang, L. Tang, M. Xie, S. Sun, W. Li, and K. Aw, "Broadband nonlinear behaviour of a soft magneto-sensitive elastomer cantilever under low-frequency and low-magnitude excitation," *J. Intell. Mater. Syst. Struct.*, vol. 29, no. 15, pp. 3165–3184, 2018.

[9] S. Zhou, J. Cao, A. Erturk, and J. Lin, "Enhanced broadband piezoelectric energy harvesting using rotatable magnets," *Appl. Phys. Lett.*, vol. 102, no. 17, p. 173901, 2013.

[10] Z. Yi, B. Yang, G. Li, J. Liu, X. Chen, X. Wang, and C. Yang, "High performance bimorph piezoelectric MEMS harvester via bulk PZT thick films on thin beryllium-bronze substrate," *Appl. Phys. Lett.*, vol. 111, no. 1, p. 013902, 2017.

[11] H. Fu and E. M. Yeatman, "Rotational energy harvesting using bi-stability and frequency up-conversion for low-power sensing applications: Theoretical modelling and experimental validation," *Mech. Syst. Signal Process.*, vol. 125, pp. 229–244, Jun. 2019.

[12] J. Wang, S. Zhou, Z. Zhang, and D. Yurchenko, "High-performance piezoelectric wind energy harvester with Y-shaped attachments," *Energy Convers. Manage.*, vol. 181, pp. 645–652, Feb. 2019.

[13] X. Mei, S. Zhou, Z. Yang, T. Kaizuka, and K. Nakano, "The benefits of an asymmetric tri-stable energy harvester in low-frequency rotational motion," *Appl. Phys. Express*, vol. 12, no. 5, p. 057002, 2019.

[14] G. Tang, B. Yang, C. Hou, G. Li, J. Liu, X. Chen, and C. Yang, "A piezoelectric micro generator worked at low frequency and high acceleration based on PZT and phosphor bronze bonding," *Sci. Rep.*, vol. 6, p. 38798, Dec. 2016.

[15] W. Liu, C. Liu, B. Ren, Q. Zhu, G. Hu, and W. Yang, "Bandwidth increasing mechanism by introducing a curve fixture to the cantilever generator," *Appl. Phys. Lett.*, vol. 109, no. 4, p. 043905, 2016.

[16] S. Li, Z. Peng, A. Zhang, and F. Wang, "Dual resonant structure for energy harvesting from random vibration sources at low frequency," *AIP Adv.*, vol. 6, no. 1, p. 015019, 2016.

[17] U. Khan and S.-W. Kim, "Triboelectric nanogenerators for blue energy harvesting," *ACS Nano*, vol. 10, no. 7, pp. 6429–6432, 2016.

[18] Y. Xi, J. Wang, Y. Zi, X. Li, C. Han, X. Cao, C. Hu, and Z. Wang, "High efficient harvesting of underwater ultrasonic wave energy by triboelectric nanogenerator," *Nano Energy*, vol. 38, pp. 101–108, Aug. 2017.

[19] Q. Shi, H. Wang, H. Wu, and C. Lee, "Self-powered triboelectric nanogenerator buoy ball for applications ranging from environment monitoring to water wave energy farm," *Nano Energy*, vol. 40, pp. 203–213, Oct. 2017.

[20] Z. Tian, J. He, X. Chen, Z. Zhang, T. Wen, C. Zhai, and C. Xue, "Performance-boosted triboelectric textile for harvesting human motion energy," *Nano Energy*, vol. 39, pp. 562–570, Sep. 2017.

[21] C. Zhai, X. Chou, J. He, L. Song, Z. Zhang, T. Wen, Z. Tian, X. Chen, W. Zhang, Z. Niu, and C. Xue, "An electrostatic discharge based needle-to-needle booster for dramatic performance enhancement of triboelectric nanogenerators," *Appl. Energy*, vol. 231, pp. 1346–1353, Dec. 2018.

[22] N. M. Kimoulakis, A. G. Kladas, and J. A. Tegopoulos, "Cogging force minimization in a coupled permanent magnet linear generator for sea wave energy extraction applications," *IEEE Trans. Magn.*, vol. 45, no. 3, pp. 1246–1249, Mar. 2009.

[23] K. Fan, S. Liu, H. Liu, Y. Zhu, W. Wang, and D. Zhang, "Scavenging energy from ultra-low frequency mechanical excitations through a bi-directional hybrid energy harvester," *Appl. Energy*, vol. 216, pp. 8–20, Apr. 2018.

[24] B. Wen, X. Tian, X. Dong, Z. Peng, and W. Zhang, "On the power coefficient overshoot of an offshore floating wind turbine in surge oscillations," *Wind Energy*, vol. 21, no. 11, pp. 1076–1091, 2018.

[25] X. Chen, H. Guo, H. Wu, H. Chen, Y. Song, Z. Su, and H. Zhang, "Hybrid generator based on freestanding magnet as all-direction in-plane energy harvester and vibration sensor," *Nano Energy*, vol. 49, pp. 51–58, Jul. 2018.

[26] T. Quan, Y. Wu, and Y. Yang, "Hybrid electromagnetic–triboelectric nanogenerator for harvesting vibration energy," *Nano Res.*, vol. 8, no. 10, pp. 3272–3280, 2015.

[27] L. Feng, G. Liu, H. Guo, Q. Tang, X. Pu, J. Chen, and C. Hu, "Hybridized nanogenerator based on honeycomb-like three electrodes for efficient ocean wave energy harvesting," *Nano Energy*, vol. 47, pp. 217–223, May 2018.

[28] W. Liu, L. Xu, T. Bu, H. Yang, G. Liu, W. Li, Y. Pang, C. Hu, C. Zhang, and T. Cheng, "Torus structured triboelectric nanogenerator array for water wave energy harvesting," *Nano Energy*, vol. 58, pp. 499–507, 2019.

[29] M. Xu, T. Zhao, C. Wang, S. L. Zhang, Z. Li, X. Pan, and Z. L. Wang, "High power density tower-like triboelectric nanogenerator for harvesting arbitrary directional water wave energy," *ACS nano*, vol. 13, no. 2, pp. 1932–1939, 2019.

[30] W. S. Hwang, J. H. Ahn, S. Y. Jeong, H. J. Jung, S. K. Hong, J. Y. Choi, and T. H. Sung, "Design of piezoelectric ocean-wave energy harvester using sway movement," *Sens. Actuators A, Phys.*, vol. 260, pp. 191–197, Jun. 2017.

[31] L. Xu, Y. Pang, C. Zhang, T. Jiang, X. Chen, J. Luo, W. Tang, X. Cao, and Z. L. Wang, "Integrated triboelectric nanogenerator array based on air-driven membrane structures for water wave energy harvesting," *Nano Energy*, vol. 31, pp. 351–358, Jan. 2017.

[32] C. Liang, J. Ai, and L. Zuo, "Design, fabrication, simulation and testing of an ocean wave energy converter with mechanical motion rectifier," *Ocean Eng.*, vol. 136, pp. 190–200, May 2017.

[33] P. Nicola, B. Giovanni, P. Biagio, S. S. Antonello, V. Giacomo, M. Giuliana, and S. Gianmaria, "Wave tank testing of a pendulum wave energy converter 1:12 Scale model," *Int. J. Appl. Mech.*, vol. 9, no. 2, p. 1750024, 2017.

[34] J. Chen, J. Yang, Z. Li, X. Fan, Y. Zi, Q. Jing, and Z. L. Wang, "Networks of triboelectric nanogenerators for harvesting water wave energy: A potential approach toward blue energy," *ACS Nano*, vol. 9, no. 3, pp. 3324–3331, 2015.

[35] S. L. Zhang, M. Xu, C. Zhang, Y.-C. Wang, H. Zou, X. He, and Z. L. Wang, "Rationally designed sea snake structure based triboelectric nanogenerators for effectively and efficiently harvesting ocean wave energy with minimized water screening effect," *Nano Energy*, vol. 48, pp. 421–429, Jun. 2018.

[36] Y.-M. Na, H.-S. Lee, and J.-K. Park, "A study on piezoelectric energy harvester using kinetic energy of ocean," *J. Mech. Sci. Technol.*, vol. 32, no. 10, pp. 4747–4755, 2018.

[37] H. Shao, Z. Wen, P. Cheng, N. Sun, Q. Shen, C. Zhou, M. Peng, Y. Yang, X. Xie, and X. Sun, "Multifunctional power unit by hybridizing contact-separate triboelectric nanogenerator, electromagnetic generator and solar cell for harvesting blue energy," *Nano Energy*, vol. 39, pp. 608–615, Sep. 2017.
[38] K. Yerrapragada, M. H. Ansari, and M. A. Karami, "Enhancing power generation of floating wave power generators by utilization of nonlinear roll-pitch coupling," *Smart Mater. Struct.*, vol. 26, no. 9, p. 094003, 2017.
[39] W. Ding, B. Song, Z. Mao, and K. Wang, "Experimental investigations on a low frequency horizontal pendulum ocean kinetic energy harvester for underwater mooring platforms," *J. Mar. Sci. Technol.*, vol. 21, no. 2, pp. 359–367, 2016.
[40] R. Rantz, M. A. Halim, T. Xue, Q. Zhang, L. Gu, K. Yang, and S. Roundy, "Architectures for wrist-worn energy harvesting," *Smart Mater. Struct.*, vol. 27, no. 4, p. 044001, 2018.
[41] Y. J. Wang, C. D. Chen, and C. K. Sung, "System design of a weighted-pendulum-type electromagnetic generator for harvesting energy from a rotating wheel," *IEEE/ASME Trans. Mechatronics*, vol. 18, no. 2, pp. 754–763, Apr. 2012.
[42] X. Zhang and Z. Ying, "Piezoelectric self-powered source of wireless bridge health monitoring nodes," in *Proc. IEEE Inf. Technol., Netw., Electron. Automat. Control Conf.*, May 2016, pp. 910–913.
[43] J. P. Carmo, J. M. Gomes, L. M. Gonçalves, and J. H. Correia, "A flexible thin-film for powering stand alone electronic devices," *Measurement*, vol. 46, no. 10, pp. 4145–4151, 2013.
[44] N. Zhao, H. Luo, P. Liang, and M. Zhou, "The design and implementation of electromagnetic vibration energy acquisition system," *Energy Procedia*, vol. 136, pp. 34–40, Oct. 2017.
[45] H. Liu, Z. Ji, T. Chen, L. Sun, S. C. Menon, and C. Lee, "An intermittent self-powered energy harvesting system from low-frequency hand shaking," *IEEE Sensors J.*, vol. 15, no. 9, pp. 4782–4790, Sep. 2015.
[46] Y. Han, Y. Feng, Z. Yu, W. Lou, and H. Liu, "A study on piezoelectric energy-harvesting wireless sensor networks deployed in a weak vibration environment," *IEEE Sensors J.*, vol. 17, no. 20, pp. 6770–6777, Oct. 2017.

YUNFEI LI received the B.Eng. degree from the School of Mechanical Engineering, Zhengzhou University, Zhengzhou, China, in 2016. He is currently pursuing the M.Eng. degree with the Robotics and Microsystems Center, School of Mechanical and Electric Engineering, Soochow University. His current research interests include practical applications in self-powered sensing and blue energy harvesting.

QIYU GUO received the B.Eng. degree from the School of Mechanical Engineering and Electric Engineering, Soochow University, Suzhou, China, in 2016, where he is currently pursuing the M.Eng. degree with the Robotics and Microsystems Center. His current research interest includes practical applications in self-powered sensing and blue energy harvesting.

MANJUAN HUANG received the B.Eng. degree in mechatronics engineering from Soochow University, Suzhou, China, in 2017, where she is currently pursuing the M.Eng. degree with the Robotics and Microsystems Center, School of Mechanical and Electrical Engineering. Her current research interest includes MEMS-based piezoelectric vibration energy harvester.

XIN MA received the B.Sc. and M.E. degrees in weapon system and utilization engineering from Northwestern Polytechnical University, Xi'an, China, in 1998 and 2005, respectively. He is currently a Senior Engineer with the Physical Oceanography Laboratory, Ocean University of China, China. His current research interests include air–sea boundary layer physical processes, ocean wave and its application, and marine environment monitoring technology.

ZHAOHUI CHEN received the B.Sc. and Ph.D. degrees in physical oceanography from the Ocean University of China, Qingdao, China, in 2007 and 2012, respectively, where he is currently a Professor with the Physical Oceanography Laboratory. His current research interests include global low-latitude equatorial currents bifurcations, dynamics of low-latitude western boundary currents, observations of multi-scale oceanic processes, building the Kuroshio Extension observation system, mobile platform development, and applications in ocean observations.

HUICONG LIU received the Ph.D. degree from the Department of Mechanical Engineering, National University of Singapore (NUS), in 2013. She was a Research Fellow with the Department of Electrical and Computer Engineering, NUS, from 2012 to 2013. She is currently a Professor with the Robotics and Microsystems Center, School of Mechanical and Electric Engineering, Soochow University, China. Her current research interests include vibration-based MEMS/NEMS energy harvesters, self-powered MEMS/NEMS system for the IoTs, and flexible functional devices for robotic and medical applications.

LINING SUN is currently the Director of the Robotics and Microsystems Center, and the President of the College of Mechatronic Engineering, Soochow University. He received the China National Funds for Distinguished Young Scientists. His current research interests include micro-nano operational robot and equipment, advanced robot and control, and electromechanical integration equipment. He received two National Science and Technology Awards Grade II and three Provincial Science and Technology Prizes Grade I. He has more than 300 academic articles being published and more than 20 patents of invention being authorized.